Bulletin of Earthquake Engineering (2021) 19:5113–5137
https://doi.org/10.1007/s10518-021-01157-2

ORIGINAL ARTICLE

Energy-based seismic design for self-centering concrete frames

Ge Song[1] · T. Y. Yang[2,3] · Ying Zhou[1]

Received: 9 December 2020 / Accepted: 11 June 2021 / Published online: 23 June 2021

Abstract

Conventional concrete frames are designed to dissipate the earthquake energy through inelastic deformation of the structural elements. It leads to hefty repairment costs and prolonged down time after earthquakes. Self-centering concrete frames (SCCF) have been introduced to minimize the unrecoverable structural damages and post-earthquake repairment costs. SCCF exhibits predictable yield mechanism and self-centering capacity. This paper presents an energy-based seismic design (EBSD) procedure for SCCFs. Based on a proposed damage model, hysteretic energy demand, E_{H}, is introduced as a key design parameter. The desired damage state and structural deformations can be considered in design process. EBSD allows designers to select various performance objectives at different seismic intensities. A prototype building is designed using the proposed EBSD procedure. The performance of SCCF designed using EBSD is compared with the same prototype structure designed using direct displacement-based design method (DDBD). The results show that SCCF has high performance with low residual drift. The performance of the EBSD designed SCCF exhibits more controlled damage compared with the DDBD designed SCCF.

Keywords Structural damages · Energy-based seismic design · Self-centering concrete frame structures · Hysteretic energy demand

1 Introduction

It has been observed in recent earthquakes that conventional systems can be designed to avoid collapse from strong earthquake shaking through inelastic deformations in structural members. Such yield mechanism results in hefty repairment costs and prolonged down time. To improve the structural performance and post-earthquake repairability,

✉ Ying Zhou
yingzhou@tongji.edu.cn

1 State Key Laboratory of Disaster Reduction in Civil Engineering, Tongji University, Shanghai 200092, China

2 International Joint Research Laboratory of Earthquake Engineering, Tongji University, Shanghai 200092, China

3 Department of Civil Engineering, University of British Columbia, Vancouver V6T1Z4, Canada

self-centering structures and components have been conceived. Critical components equipped with post-tensioned (PT) tendons and energy-dissipation devices have been proposed to enhance the structural performance of existing structures. (Barbagallo et al. 2020; Wang et al. 2020, 2021; Cai et al. 2021; Xue et al. 2021; Wu et al. 2021;). Meanwhile, self-centering moment frame structures have been developed (Priestley et al. 1993; Cheok et al. 1994; EL-Sheikh et al. 1999; El-Sheikh et al. 2000; Korkmaz et al. 2005) to upgrade aseismic performance of conventional frames. These systems exhibit excellent performance, where the structures can be functional immediately or shortly after strong earthquake shaking. The self-centering concrete frame (SCCF) originally proposed by Priestley and Tao (1993) is one such system. SCCF uses PT tendons and yielding components at the beam-column connections to dissipate earthquake energy and provide the self-centering mechanism. SCCF is commonly designed using the direct displacement-based design (DDBD) method (Priestley et al. 2002). DDBD focuses on the use of maximum deformation as the main design parameter to satisfy the strength and deformation requirements. Unlike conventional concrete frames, SCCF is more sensitive to the cumulative effect and residual deformation (Zhou et al. 2020a). Hence, it is more rational to utilize an energy-based design approach for SCCF structures.

Energy-balance concept was first introduced by Housner in the first world conference on earthquake engineering (Housner et al. 1959). The input energy from earthquakes, E_{I}, is mainly dissipated through damping energy, E_{D}, and hysteresis energy, E_{H}. While the remaining energy is stored in the system as kinetic energy E_{K} and elastic strain energy E_{s}. Equation (1). shows the energy-balance concept (Uang et al. 1990).

$$E_{\mathrm{I}} = E_{\mathrm{D}} + E_{\mathrm{H}} + E_{\mathrm{K}} + E_{\mathrm{S}} \tag{1}$$

Many researchers have proposed energy-based design methods for different structural systems. Akiyama (1985) illustrated a systematic design procedure based on the energy-balance concept, and it has been implemented in a technological standard for earthquake-resistant calculation method in Japan since 2005 (2005). Fajfar et al. (1996) proposed the N2 method and modified Park-Ang model for the design and performance evaluation for conventional concrete frames. Akbas et al. (2001) conducted statistical analyses to study energy input and dissipation. Since the study was performed based on small sample set and a linear distribution of energy dissipation along structural heights was adopted, energy features could not be evaluated precisely. Chou et al. (2003) studied the distribution of E_{H} via multi-pushover analyses (MPA) method and proposed an energy-based design approach. It has been proved that the seismic energy is not only related to structural features, but also ground motion characteristics, including peak values, frequency and duration (Zhou et al. 2019a). Since the MPA method is a static methodology for structure analyses, it cannot accurately capture the real structural behaviors and responses under seismic actions. Thus, the applicability of MPA still remains to be discussed. Meanwhile, Yang et al. (2018; 2020) proposed an equivalent energy design procedure, which allows designers to select various performance objectives for different seismic intensities. It enables structures achieve desired strength and deformation without iterations in the design procedure.

Since the energy-based design procedure specific to self-centering concrete frame structures is still limited, an energy-based design method to routinely design SCCFs is needed. Several specific subjects, including the energy spectra, the damage evaluation and the energy distribution within SCCFs have been investigated in previous researches (Zhou et al. 2020a, b; Song et al. 2021). In this paper, a newly conceived energy-based seismic design (EBSD) procedure for SCCF structures is presented. Based on the proposed damage model, the hysteretic energy demand E_H is introduced as a key design parameter for SCCFs. The proposed design procedure considers not only the deformation and energy demands of SCCFs, but also the desired damage states, which would limit the damage development in the well-designed structures. In addition, it allows designers to select various performance objectives for different seismic intensities satisfying with multiple performance levels.

2 Energy-based seismic design procedure

The first step of the proposed EBSD is to determine the E_I and E_H for the whole structure from the design energy spectra. The second step of EBSD is to quantify the hysteretic energy demand for the critical components E_{Hi}. Then, E_{Hi} is converted as a key design index. The last step of EBSD is to select the critical design parameters, including the maximum deformation θ_m, the recoverable deformation θ_r, the ultimate deformation θ_u and damage index DI, to achieve multi-performance objectives.

2.1 Energy-dissipation mechanism for SCCF

Figure 1 shows the yield mechanism of SCCF with typical beam-column joints, known as hybrid joints (Cheok et al. 1993; ACI 2003). The hybrid joint has: (a) equal moment strength for top and bottom energy-dissipating mild steels; (b) unbonded PT tendons that connected the beams to the columns through the centroid of the beam. NIST program (Cheok et al. 1993) showed that a well-designed hybrid joint has sufficient strength, stiffness and energy-dissipation capacities, while exhibiting great self-centering behaviors under cyclic loads. The nonlinearity occurred in mild steels can dissipate seismic energy to protect critical components from sever damages. This leads to stable and controllable damage development.

2.2 Quantification of E_H

The quantification of energy demands includes determining E_H and its distribution within structures. Normally, the energy demand for different systems can be derived from input energy spectra and hysteretic energy spectra (Zhou et al. 2019a, b). It has been demonstrated that both the ground motion types and structural features have great effects on E_I (Decanini et al. 1998; Chou et al. 2000; Cruz et al. 2000), while the hysteretic model should be considered in determining E_H (Zhou et al. 2019b). Therefore, the applicability

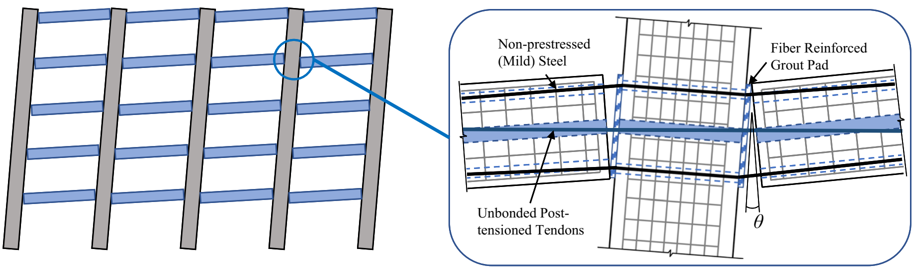

Fig. 1 Yielding mechanism of SCCF

of existing energy spectra needs to be considered in the quantification of E_I and E_H for SCCFs. Meanwhile, for implementing the design method into component level, quantification of the energy demands for critical components E_{Hi} are needed after determining E_H for the whole system.

2.2.1 Energy spectra

Zhou et al. (2020b) proposed a practical design energy spectrum for self-centering systems. The proposed energy spectra are applicable to different site class stipulated in the Chinese code (2016) and can consider the influences of ground motion types and structural characteristics.

Equivalent velocity, *Ve*, as shown in Eq. (2), is adopted as the input energy per unit mass of structures (Zhou et al. 2020b):

$$Ve = \sqrt{\frac{2E_I}{m}} \tag{2}$$

where m represents the mass of the system.

Figure 2 shows the flag-shaped hysteretic model adopted in the study to model seismic responses of self-centering systems (Zhou et al. 2020b). M_y and θ_y represent the yield strength and deformation, respectively. K represents the initial stiffness, α represents the post-yield stiffness ratio, η represents the ratio of the yield strength. θ_u represents the maximum deformation. The ductility factor μ, which defined as θ_u/θ_y, was adopted to define the nonlinear behaviors of systems and to construct the constant-ductility spectra.

In order to predict *Ve* of different systems, a benchmark model with $\eta=0.4$, $\xi=0.02$, $\mu=2$ and $\alpha=0.2$ is adopted in the study, where ξ is the damping ratio. Design spectrum of the benchmark model is denoted as $Ve_{\text{benchmark}}$. The design spectrum of target systems with different η, ξ, μ and α can be constructed based on $Ve_{\text{benchmark}}$. The proposed design spectra are divided into three portions as a function of the vibration period. Figure 3 illustrates the construction of design spectrum for the benchmark model (Zhou et al. 2020b).

Fig. 2 Flag-shaped hysteretic model

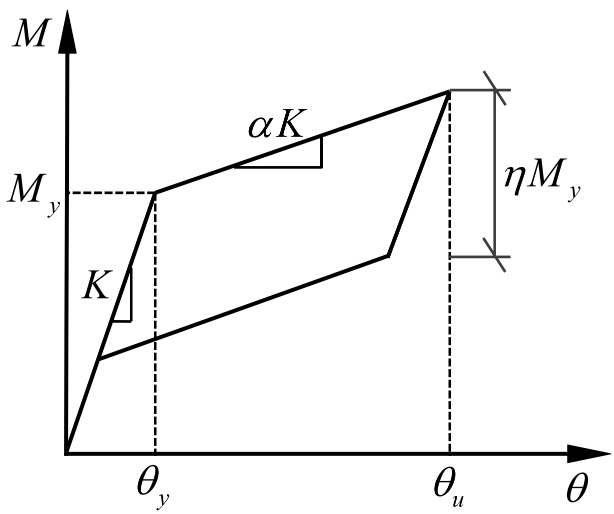

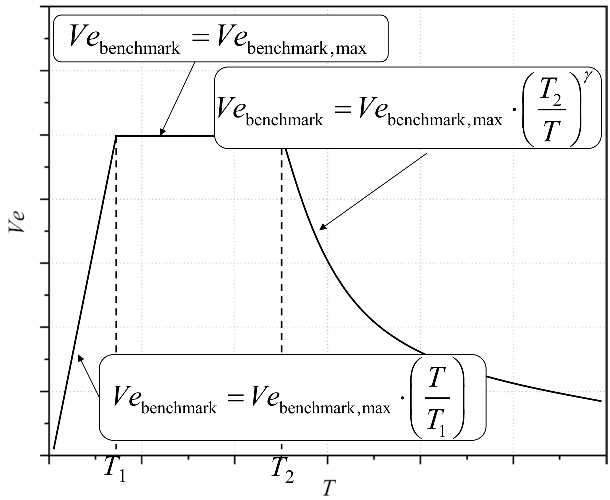

Fig. 3 Construction of design spectra for $Ve_{\text{benchmark}}$

Where $Ve_{\text{benchmark, max}}$ is the peak value of the design spectrum; T_1, T_2 are characteristic periods related to ground motion types; γ is the fitting parameter.

It has been demonstrated that input energy spectra closely relate to ground motion features (Zhou et al. 2019a; Zhou et al. 2020b). According to the Chinese code (2016), ground motions are divided into 12 types according to site types (I ~ IV) and design groups (1 ~ 3). Site types are classified based on the shear wave velocity of soil, while design groups are defined by characteristic period. Detailed information can be obtained from the code (2016). Figure 4 illustrates $Ve_{\text{benchmark}}$ corresponding to different site types and design groups constructed according to Fig. 3 (Zhou et al. 2020b).

Figure 5 illustrates the design input energy spectrum for self-centering systems with different structural features and seismic intensities. It is constructed based on the $Ve_{\text{benchmark}}$ presented in Figs. 3 and 4. τ, ρ, φ and λ are the corresponding correction factors related to structural features. detailed information of τ, ρ, φ and λ can be derived from the reference (Zhou et al. 2020b). Results showed that the proposed procedure can reasonably predict the input energy for self-centering systems (Zhou et al. 2020b). E_{I} of the system can be derived from Eq. (2).

As for E_{H}, Zhou et al. (2020b) proposed $E_{\text{H}}/E_{\text{I}}$ spectra to determine the hysteretic energy demand E_{H} for self-centering systems. Equation (3) gives the method to calculate the target E_{H} / E_{I} spectrum. The results show that the proposed E_{H} / E_{I} spectrum can give a reliable estimation of E_{H} / E_{I} for self-centering systems. E_{H} of the target system can be derived from the E_{H} / E_{I} spectrum. Detailed information can be obtained from the reference.

$$\left(E_{\text{H}}/E_{\text{I}}\right)_{\xi,\mu,\eta} = 0.35 I_1 \cdot I_2 \cdot I_3 \tag{3a}$$

$$I_1 = 5.75 \cdot \xi^{0.28} \cdot \eta^{1.06+0.17\cdot\ln(\xi-0.0087)} \tag{3b}$$

$$I_2 = (0.014 + 0.08\eta) \cdot \xi^{-0.56-0.52\cdot0.23^{\eta}} \tag{3c}$$

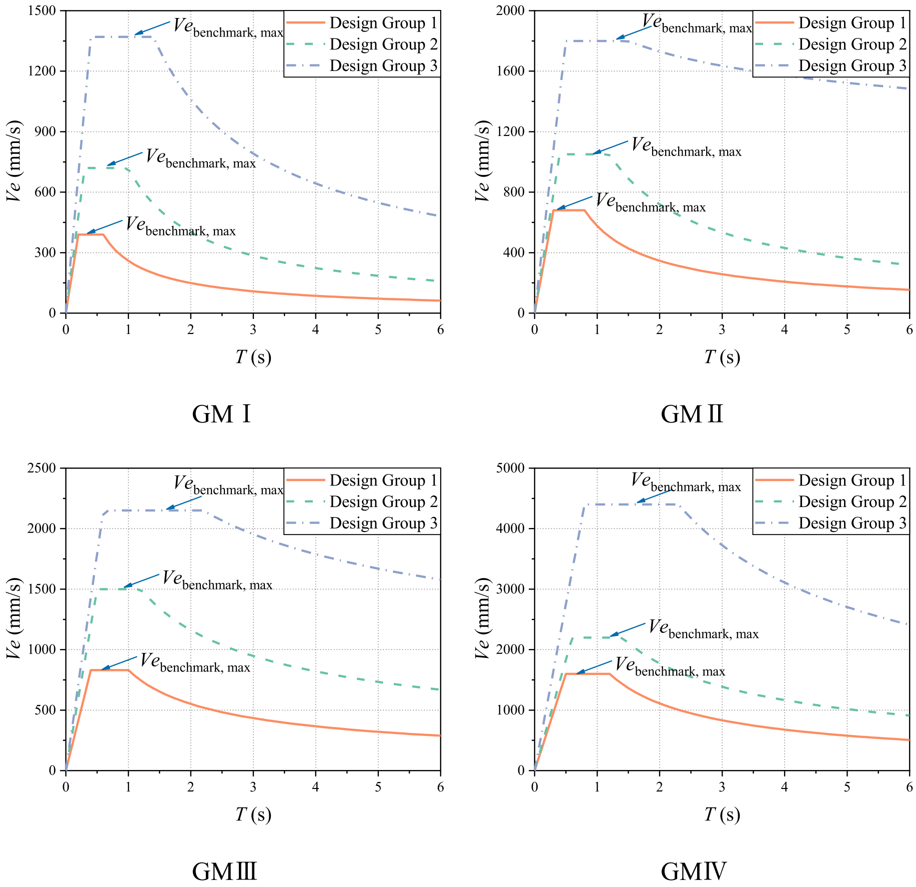

Fig. 4 Design spectra for $Ve_{\text{benchmark}}$

Fig. 5 Design Ve spectrum

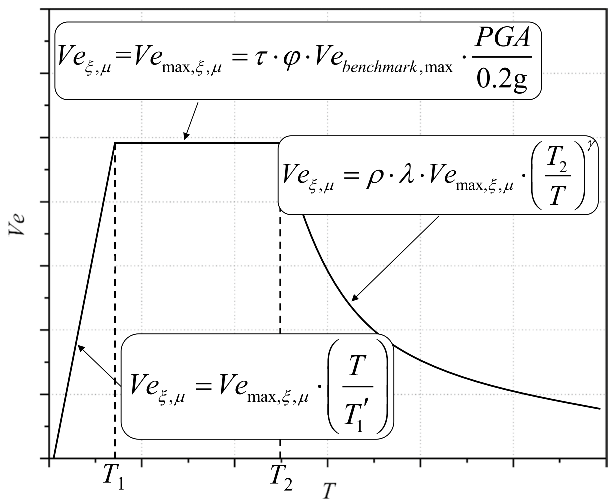

Table 1 Fitting results for distribution of E_H

A_{i1}	A_{i2}
$A_{11} = 1.399 - 0.002e^{\frac{n}{1.819}}$	$A_{12} = 0.021 + 15.410e^{-\frac{n}{2.033}}$
$A_{21} = 5.543 - 2.058n + 0.129n^2$	$A_{22} = -1.259 - 158.602e^{-\frac{n}{1.671}}$
$A_{31} = 2.002 - 1428.335e^{-\frac{n}{0.792}}$	$A_{32} = 2.009 + 193.117e^{-\frac{n}{1.899}}$
$A_{41} = -1.046 + 10.866e^{-\frac{n}{2.897}}$	$A_{42} = -0.286 - 53.294e^{-\frac{n}{2.569}}$

Table 2 Fitting results for $E_{Hn,\ joint}$ / $E_{H,\ joint\_all}$

A_{i1}	A_{i2}
$A_{11} = 0.228 - 0.002e^{\frac{n}{2.029}}$	$A_{12} = -0.839 + 0.00094e^{\frac{n}{1.444}}$
$A_{21} =$ - $0.065 + 0.013n$	$A_{22} = 0.893 - 0.109n$

$$I_3 = A + B \cdot T + C \cdot T^2 \tag{3d}$$

$$A = 0.35 + 0.52 \cdot \mu - 0.06 \cdot \mu^2 \tag{3e}$$

$$B = -0.11 \cdot \ln(\mu - 1.19) \tag{3f}$$

$$C = 0.02 - 0.04 \cdot 0.80^{\mu} \tag{3g}$$

2.2.2 Distribution of E_H in structures

Many theoretical and numerical studies have been conducted to quantify energy distribution in conventional systems (Bojorquez et al. 2008; Lopez-Barraza et al. 2016; Du et al. 2019; Tu et al. 2018). Song et al. (2021) evaluated the distribution of E_H in self-centering frame structures with various structural features and heights. Empirical equations were established to quantify the hysteretic energy demands for hybrid joints, as shown in Eq. (4) and Table 1.

$$\begin{aligned} E_{Hi,joint}/E_{H,joint\_all} = {} & (A_{11} + A_{12} \cdot PGA)\frac{H_i}{H} + (A_{21} + A_{22} \cdot PGA)(\frac{H_i}{H})^2 \\ & + (A_{31} + A_{32} \cdot PGA)(\frac{H_i}{H})^3 + (A_{41} + A_{42} \cdot PGA)(\frac{H_i}{H})^4 \end{aligned} \tag{4}$$

where $E_{Hi,\ joint}$ is the hysteretic energy demand of hybrid joints at the i-th floor; $E_{H,\ joint\_all}$ is the energy demand of all hybrid joints; H_i/H is the height of each floor normalized by the total height of the structure; n is the total number of the floor. Meanwhile, the results showed that self-centering parameter λ has non-negligible effects on $E_{Hi,\ joint}$ when $PGA \leq 0.2$ g, especially $E_{Hi,\ joint}$ of the top floor, denoted as $E_{Hn,\ joint}$. A modified method was suggested to estimate $E_{Hn,\ joint}$ / $E_{H,\ joint\_all}$ considering λ, as shown in Eq. (5) and Table 2. It has been demonstrated that the proposed approaches can be adopted to quantify the distribution of E_H within SCCFs appropriately (Song et al. 2021).

$$E_{Hn,joint}/E_{H,joint\_all} = (A_{11} + A_{12} \cdot PGA) + (A_{21} + A_{22} \cdot PGA) \cdot \lambda \tag{5}$$

It should be noted that NZS3101:2006 (2006) uses self-centering parameter λ to consider relations between the self-centering property and the energy-dissipation capacity. It is defined as the ratio of resisting moment attributed from PT tendons M_{PT} to that of mild steels M_{S}, as:

$$\lambda = \frac{M_{\mathrm{PT}}}{M_{\mathrm{s}}} \geq 1.0 \tag{6}$$

Normally, $\lambda = 1 \sim 2$ is adopted as a key index to design the basic relation between self-centering and energy-dissipation capacities for SCCFs (Pampanin et al. 2010). However, as discussed in Sect. 2.2.1 and Fig. 3, η is defined as the ratio of the yield strength to represent the energy-dissipation capacity in the proposed energy spectra, which can be obtained from Eq. (7a) (Pampanin et al. 2010). In order to switch λ and η in design procedures, the relation of λ with η can be given based on Eq. (6) and Eq. (7a) as:

$$\eta = \frac{2M_{\mathrm{S}}}{M_{\mathrm{S}} + M_{\mathrm{PT}}} \tag{7a}$$

$$\eta = \frac{2}{\lambda + 1} \tag{7b}$$

2.3 Conversion of the hysteretic energy demand as a design parameter

In order to consider the effect of the hysteretic energy demand on the structural performance and the damage development, it needs to be converted as a design parameter in EBSD. Zhou et al. (2020a) proposed a damage model composing of structural deformations and the hysteretic energy demand of hybrid joints E_{Hjoint} to quantify the damage development in hybrid joints, as shown in Eq. (8).

$$\mathrm{DI}_{\theta_{\mathrm{c}}} = \frac{\theta_{\mathrm{m}} - \theta_{\mathrm{r}}}{\theta_{\mathrm{u}} - \theta_{\mathrm{r}}} = \frac{\theta_{\mathrm{c}}}{\theta_{\mathrm{u}} - \theta_{\mathrm{r}}} \tag{8a}$$

$$\mathrm{DI}_{E_{\mathrm{H}}} = \beta \frac{E_{\mathrm{Hjoint}}}{M_{\mathrm{y}}\theta_{\mathrm{u}}} \tag{8b}$$

$$\mathrm{DI} = \mathrm{DI}_{\theta_{\mathrm{c}}} + \mathrm{DI}_{E_{\mathrm{H}}} \tag{8c}$$

where E_{Hjoint} represents the hysteretic energy demand of hybrid joints under cyclic loads; θ_{m} and θ_{r} are the maximum and recoverable deformation, respectively; θ_{u} represents the ultimate deformation under monotonic loads; M_{y} represents the design moment for hybrid joints, which generally corresponds to the state when PT tendons yield; β represents a non-negative factor related to energy-dissipation capacity; $\theta_{\mathrm{c}} = \theta_{\mathrm{m}}$—$\theta_{\mathrm{r}}$ represents the residual deformation of the structure. Equation (9) can be used to quantify θ_{u} for hybrid joints (El-Sheikh et al.2000).

$$\theta_u = \frac{\varepsilon_{cc}}{c} \cdot L_{cr} \tag{9a}$$

$$L_{cr} = \min\left\{2c\beta', b''\right\} \tag{9b}$$

where ε_{cc} represents the ultimate strain of the confined concrete; c represents the compression height of the beam; L_{cr} represents the length of the plastic hinge developed along the beam; β' is the coefficient corresponding to the concrete compression height; and b'' is the width of the confined concrete.

Equation (8) can be re-written as:

$$M_y = \frac{\beta E_{\text{Hjoint}}}{(\text{DI} - \frac{\theta_c}{\theta_u - \theta_r})\theta_u} \tag{10}$$

It can be seen that Eq. (10) converts E_{Hjoint} as a design parameter by relating M_y with E_{Hjoint} and the deformation responses. Meanwhile, the structural damage state under certain seismic intensities can also be considered by selecting desired damage index DI.

As discussed in the reference (Zhou et al. 2020a), β closely relates to structural features and has great effects on the damage evaluation. Zhou et al. (2020a) proposed Eq. (11) to determine β for hybrid joints.

$$\beta = 0.0742(1.444\rho_v - 0.935)(0.736 + 0.171\lambda)(0.026f_c - 0.213) \tag{11}$$

where ρ_v represents the stirrup reinforcement ratio at beam ends, f_c represents the concrete strength.

2.4 Determination of critical design parameters

To achieve multi-performance objectives, DI, θ_m, θ_r, and θ_c in Eq. (10) need to be quantified corresponding to different requirements. Zhou et al. (2020a) investigated the damage development and suggested damage intervals for hybrid joints, as shown in Table 3. Compared with damage intervals presented by Park–Ang for conventional concrete structures (Park et al. 1985), the damage limits corresponding to different damage states are extended, implying the superiorities in the performance improvement and damage control of self-centering systems (Zhou et al. 2020a). Meanwhile, it has been demonstrated that well-designed hybrid joints can limit structural damages within the joint and prevent other critical components from severe damages.

According to Eq. (10), smaller DI indicates less damages in the hybrid joints, which results in bigger M_y. Designers are free to choose a DI for desired damage states under target seismic intensity.

The damage development and behaviors of 29 hybrid joints under cyclic loads were analyzed to investigate deformation indexes (Zhou et al. 2020a). The results showed that

Table 3 Damage intervals for hybrid joints

Damage state	Damage interval
No damage	[0, 0.1)
Minor damage	[0.1, 0.3)
Moderate damage	[0.3, 0.5)
Severe damage	[0.5, 0.9)
Collapse	[0.9, $+\infty$)

θ_c under minor damage states were all less than 0.1%, while θ_m corresponding to a minor earthquake was suggested based on the Chinese building code (2016) (Zhou et al. 2020a). According to the study, $\theta_c = 0.2\%$ was adopted for DBE to ensure the minor damage state and structural integrity (Zhou et al. 2020a). Meanwhile, ACI T1.2–03 recommend $\theta_m = 3.5\%$ to ensure the stability of force transferring under MCE (ACI 2003). In addition, to satisfy with the repairable performance objective for MCE, $\theta_c = 0.4\%$ was adopted to control the damage developed in structures. Zhou et al. (2020a) suggested the damage-based deformation indexes for hybrid joints, as listed in Table 4, where DBE represents the design-based earthquake, MCE represents the maximum considered earthquake. Detailed information can be derived from the reference (Zhou et al. 2020a).

Although θ_m, θ_c are suggested in Table 4, designers can select other values for various performance objectives based on reliable analyses.

2.5 Determination of design rotations for hybrid joints

Story drift θ_i is normally adopted as the design index, which is different from rotations of hybrid joints θ_n. In this case, θ_n need to be converted from story drifts θ_i in the design procedure. The method elaborated in PRESSS Design Handbook (2010) is adopted in this paper to obtain rotations for hybrid joints.

A normalized nonlinear mode deformation δ_i is adopted to elaborate the deformed shape at the peak displacement response (Pampanin et al. 2010). For frames higher than four floors, an inelastic mode deformation is defined by Priestley et al. (2002), as shown in Eq. (12).

$$\delta_{\mathrm{i}} = \frac{4}{3}\left(\frac{H_i}{H_n}\right)\left(1 - \frac{H_i}{4 \cdot H_n}\right) \tag{12}$$

The target displacement at the i-th floor can be given as:

$$\Delta_{\mathrm{i}} = \delta_{\mathrm{i}}\left(\frac{\Delta_{\mathrm{c}}}{\delta_{\mathrm{c}}}\right) \tag{13}$$

where δ_c is the normalized displacement of the first floor obtained from Eq. (12); Δ_c is the displacement of the first floor.

According to the design handbook (2010), the story drift θ_i can be divided as the sum of the yielding drift θ_y and the beam rotation θ_p. Priestley has noted that for frames utilizing unbonded post-tensioned tendons (Priestley 2002), θ_y can be obtained as:

$$\theta_{\mathrm{y}} = 0.0004\left(\frac{L_{\mathrm{b}}}{h_{\mathrm{b}}}\right) \tag{14}$$

where L_b and h_b are the length and height of beams.

Table 4 Performance-based deformation indexes

Deformation index	Minor earthquake	DBE	MCE
Maximum deformation (%)	0.18	2	3.5
Residual deformation (%)	0.1	0.2	0.4

Therefore, the rotation of the hybrid joint θ_n can be derived from the following equation (Pampanin et al. 2010):

$$\theta_p = \theta_i - \theta_y \tag{15a}$$

$$\theta_n = \frac{\theta_p}{1 - \frac{h_c}{L_b}} \tag{15b}$$

where h_c is the height of column sections.

Figure 6 presents the flow chart of the EBSD procedure for SCCF proposed in this paper. The procedure has three steps: determination of design parameters, capacity design for critical components and evaluation of structural performance. It allows designers to select different performance objectives based on desired damage states and deformation responses at target seismic intensities.

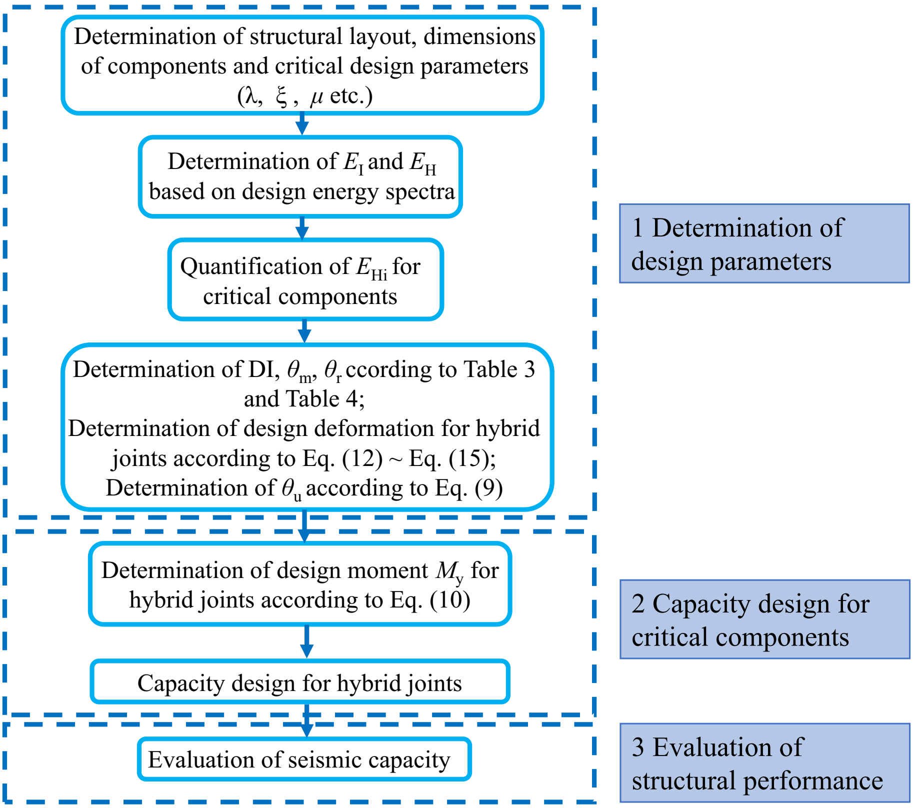

Fig. 6 Flow chart for EBSD

3 Application of EBSD

To demonstrate the applicability of EBSD, the concrete building presented in the PRESSS Design Handbook (2010) is adopted as the prototype building. A five-story SCCF and an eight-story SCCF are designed using both the EBSD and DDBD procedures under different hazard levels. Seismic performances of the design examples are compared by nonlinear dynamic analyses.

3.1 Prototype building

The prototype building is assumed to be located in areas where the Site Class is classified as II according to the Chinese building code (2016). The characteristic period $T_g = 0.4$ s. Figure 7a shows the plan view of the prototype building. The building includes two types of seismic force resisting systems: SCCF in the East–West direction and self-centering shear walls in the North–South direction. In this paper, only the SCCF in the East–West direction

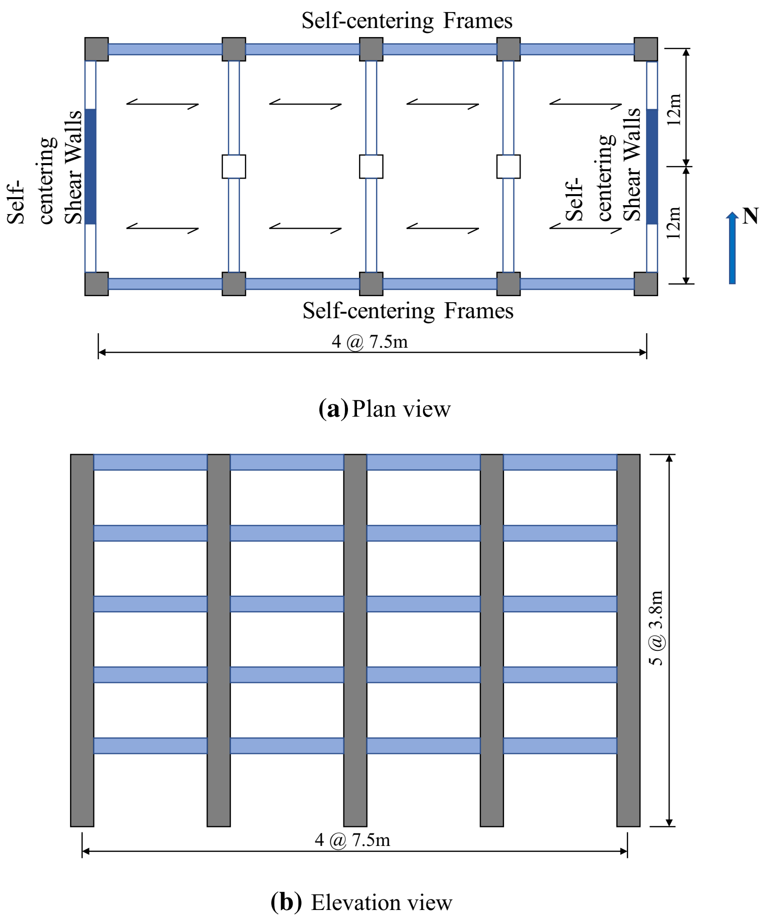

Fig. 7 Geometry of the prototype building

Table 5 Material properties

Material properties	
Concrete	
Concrete compression strength, f_c	40 MPa
Confinement ratio, f_{cc}/f_c	1.25
Ultimate concrete strain, ε_{lim}	0.02
Modulus of ealsticity, E_c	32000 MPa
Post-tensionend Steel	
15.2 mm diameter super strands	
Area of tendom, A_{pt}	143.3mm2
Modulus of ealsticity, E_{pt}	200000 MPa
Yield stress (0.1% proof stress), f_{pty}	1560 MPa
Ultimate stress, f_{ptu}	1750 MPa
Mild steel	
Modulus of ealsticity, E_s	195000 MPa
Yield stress, f_y	300 MPa
Yield strain, ε_y	1500με
Bilinear strain hardening ratio, r	0.80%
Ultimate strain, ε_{lim}	50000με
Unconfined concrete	30 mm
Stirrups	12 mm

Table 6 Design rotation for hybrid joints in the five-story structure

Level	Design displacement at the i-th floor Δ_i (mm)	Inter-story drift θ_i(%)	Beam rotation θ_p (%)	Design rotation of hybrid joints θ_n (%)
5	300	1.16	0.70	0.77
4	256	1.37	0.91	1.00
3	204	1.58	1.12	1.23
2	144	1.79	1.33	1.46
1	76	2.00	1.54	1.70

is designed and examined. The elevation view of the frame is presented in Fig. 7b. Dimensions of beams and columns are 400 mm × 650 mm and 700 mm × 700 mm for both EBSD and DDBD designed structures.

In order to validate the applicability of the proposed design procedure, different hazard levels are adopted for different design examples. The five-story SCCF is designed assuming the seismic fortification intensity equaling to 7 degree according to the Chinese building code (2016), while that of the eight-story SCCF is 8 degree. It should be noted that all material and dimension information are the same for both the five-story and eight-story design examples.

Table 5 lists the material properties of the prototype building. They are adopted for both EBSD and DDBD designed structures.

In this paper, the inter-story drift limit is selected as 2% for both design examples in EBSD and DDBD design procedures. λ is chosen as 2 to ensure a full re-centering capacity for the system. Design deformations of two SCCFs are given in Tables 6 and 7. They

Table 7 Design rotation for hybrid joints in the eight-story structure

Level	Design displacement at the *i*-th floor Δ_i (mm)	Inter-story drift θ_i(%)	Beam rotation θ_p (%)	Design rotation of hybrid joints θ_n (%)
8	471	1.10	0.64	0.70
7	429	1.23	0.77	0.84
6	382	1.35	0.89	0.99
5	331	1.48	1.02	1.13
4	275	1.61	1.15	1.27
3	213	1.74	1.28	1.41
2	147	1.87	1.41	1.56
1	76	2.00	1.54	1.70

are adopted in both the EBSD and DDBD procedures. Design rotations of hybrid joints θ_n at each floor are summarized in Tables 6 and 7. Δ_i is calculated according to Eq. (12) and Eq. (13). θ_n is calculated based on Eq. (14) and Eq. (15).

3.2 Structure design

3.2.1 Determination of design parameters

According to Sect. 2 and Fig. 1, the design energy spectrum needs to be determined first. As discussed in Sect. 2.2, the ductility factor μ is adopted for defining nonlinear behaviors of systems and constructing constant-ductility spectra. Priestley (1999) noted that for jointed precast systems, superior ductility can be guaranteed compared with traditional concrete systems. An allowable limit of $\mu = 6$ can be selected for frame structures. For both design examples, $\theta_y = 0.51\%$ and $\theta_u = 3.4\%$ can be calculated according to Eq. (14), Eq. (15) and Eq. (9). The resultant $\mu = 6.67$. Hence, $\mu = 6$ is adopted to construct energy spectra for both design examples in this case. According to Eq. (7), $\eta = 0.67$.

Based on the calculated structural features and the proposed design energy spectra shown in Fig. 5 and Eq. (3), key parameters of the target energy spectra for both the examples are summarized in Table 8. Design energy spectra can be obtained according

Table 8 Target design energy spectra

Input energy spectrum		*E*H / *E*I spectrum	
Parameter	Value	Parameter	Value
φ	0.936	I_1	2.01
τ	0.887	I_2	0.652
ρ	0.915	I_3	1.686–0.17 T + 0.013T2
T_1’	0.258		
$Ve_{benchmark,max}$ (mm/s)	1050		
Ve_{max} (mm/s) (Five-story SCCF)	959		
Ve_{max} (mm/s) (Eight-story SCCF)	1744		

to procedures elaborated in Sect. 2.2.1. Figure 8 present the design energy spectra for both the five-story and eight-story SCCFs.

Table 9 lists the main energy indexes of the two design examples.

As discussed in Sect. 2.2, results of $E_{Hi, joint}$ / $E_{H, joint\_all}$ for both the five-story and eight-story design examples are listed in Tables 10 and 11. In this paper, the maximum of $E_{Hi, joint}/E_{H, joint\_all}$ is adopted for hybrid joints at each floor to conservatively design the structure. Thus $E_{Hi, joint}/E_{H, joint\_all} = 0.261$ and $E_{Hi, joint}/E_{H, joint\_all} = 0.171$ are adopted for the two design examples, respectively. It has been demonstrated that for self-centering frames, the energy demand can be equally distributed among hybrid joints at the same floor (Song et al. 2021). Since there are a total of eight joints per floor, the energy demand is about 1/8 of all joints at the same floor. Thus, the energy demand of each hybrid joint is $E_{Hjoint} = 72$ KN·m in the five-story SCCF, while $E_{Hjoint} = 109$ KN·m in the eight-story SCCF.

According to Tables 3 and 4, DI = 0.5 and $\theta_c = 0.4\%$ are selected to limit the damage development for the repairable requirement after seismic actions in both design examples. The recoverable deformation $\theta_r = 0.834\%$.

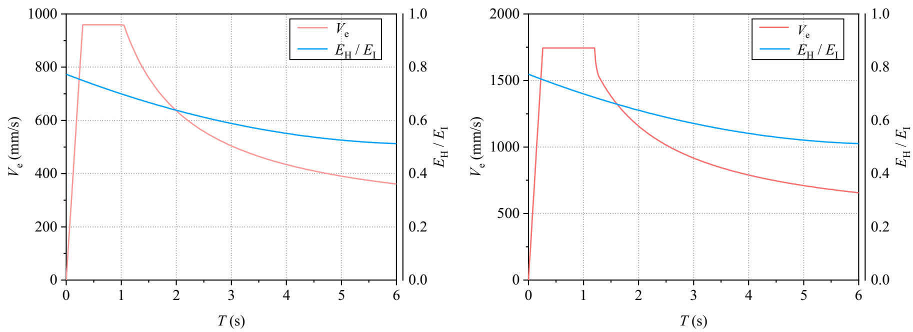

(a) Five-story structure **(b)** Eight-story structure

Fig. 8 Design energy spectra

Table 9 Energy indexes

Energy indexes	Five-story SCCF	Eight-story SCCF
E_I (KN·m)	4255	9795
E_H (KN·m)	2919	6238
$E_{H, joint\_all}$ (KN·m)	2199	5122

Table 10 $E_{Hi, joint}$ / $E_{H, joint\_all}$ for the five-story SCCF

H_i / H	$E_{Hi, joint}$
0	0
0.2	0.212
0.4	0.261
0.6	0.236
0.8	0.197
1	0.168

Table 11 $E_{Hi, joint}$ / $E_{H, joint\_all}$ for the eight-story SCCF

H_i / H	$E_{Hi, joint}$
0	0
0.125	0.121
0.25	0.167
0.375	0.171
0.5	0.156
0.625	0.140
0.75	0.132
0.875	0.129
1	0.125

3.2.2 Capacity design for critical components

Based on Eq. (10), the design moment of hybrid joints can be calculated. Table 12 lists design moments of both design examples using EBSD and DDBD procedures (Priestley 2002).

Reinforcement design for hybrid joints is performed according to NZS3101 Appendix B (2006). Detailed reinforcement information for all design examples is presented in Table 13.

M_{hybrid}—θ responses for a typical hybrid joint can be derived from that contributed by PT tendons M_{PT} and mild steels $M_{S.}$ Four performance points, including decompression, MS yield, PT yield and ultimate limit, can be calculated based on reinforcement properties listed in Table 13. The procedure elaborated in the PRESSS Design Handbook (2010) is adopted to calculate corresponding M_{hybrid}, M_{PT} and M_S. Table 14 and Fig. 9 summarize the moment-rotation co-ordinates of the EBSD and DDBD designed hybrid joints for the two design examples. It can be seen from the table that the EBSD designed structures require higher design moments than that of the DDBD designed structures. Since the cumulative effect is considered in the EBSD, bigger design strength shall be needed in the EBSD designed structures to limit damages developed in structures.

4 Evaluation of seismic performance

4.1 Numerical modeling

Figure 10 shows the modeling of the hybrid joint developed in *OpenSees* (2000). The hybrid model was developed using zero-length spring element. ElasticMultilinear material in *OpenSees* was selected to simulate M_{PT}—θ responses. Steel02 material is adopted to model M_S—θ responses. The hysteretic behavior of hybrid joints can be obtained by combining two materials with parallel command.

A displacement-based fiber element is used to model the column. The length of the element, where the plastic hinge formed during earthquakes L_{cr}, can be calculated according

Table 12 Design moments for hybrid joints

Design moment (KN·m)	EBSD	DDBD
Five-story SCCF	405.686	342.404
Eight-story SCCF	613.694	532.872

Table 13 Detailed information of reinforcement for hybrid joints

Model		Hybrid Joint					λ for Hybrid Joint	λ for Structure
		PT Number	Initial PT Force (KN)	Initial PT Stress ($/ f_{PTu}$)	Mild Steel Type	Mild Steel Number (each)		
Five-story	DDBD	6	808	0.54	D22	2	2.07	2.10
SCCF	EBSD	7	960	0.55	D22	3	2.08	2.13
Eight-story	DDBD	9	1267	0.56	D24	3	2.03	2.12
SCCF	EBSD	10	1471	0.59	D26	3	2.05	2.11

Table 14 Moment-rotation co-ordinates for hybrid joints

		Rotation (%)		M_s (KN·m)		M_{pt} (KN·m)		M_{hybrid} (KN·m)	
		DDBD	EBSD	DDBD	EBSD	DDBD	EBSD	DDBD	EBSD
Five-story structure	Decompression	0	0	0	0	87.5	104	87.5	104
	MS yield	0.104	0.105	116	174	210	249	326	422
	PT yield	1.234	1.234	129	190	273	318	401	509
	Ultimate limit	3.400	3.400	129	190	273	318	401	509
Eight-story structure	Decompression	0	0	0	0	153	159	153	159
	MS yield	0.115	0.115	206	242	359	375	565	617
	PT yield	1.200	1.200	221	258	446	460	667	718
	Ultimate limit	3.400	3.400	221	258	446	460	667	718

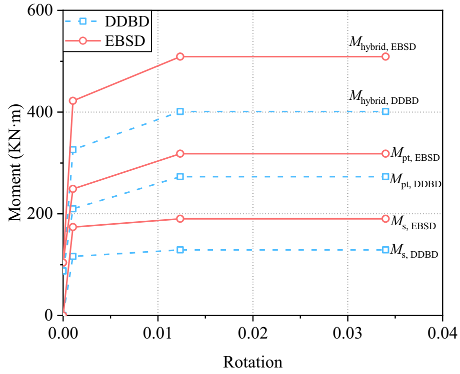

(a) Five-story structure

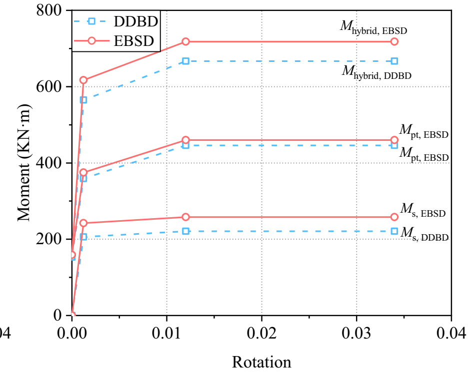

(b) Eight-story structure

Fig. 9 Moment-rotation co-ordinates for hybrid joints

to Eq. (9). Behaviors of mild steels are modeled by Steel02 with CorotTruss elements. Since mild steels are debonded for a length through the lower part of columns, rigid links are used to model relative relations between columns and mild steels. Rayleigh damping model is utilized based on 5% of critical damping ratio to the first and third modes of models. Table 15 shows the first three modal period of the EBSD and DDBD designed structures.

The columns and beams are capacity designed to remain elastic, while all the nonlinearities are concentrated at the joint zones and at the base of columns at the first floor. Therefore, only nonlinearities of the joints and column based are modeled, while beams and columns are constructed with elastic elements. Post-processing has been performed to guarantee these elements remain elastic after seismic actions.

The experimental data of M-P-Z4 and O-P-Z4 specimens obtained from the NIST program (Cheok et al. 1993) are adopted to validate the modeling approaches discussed above. Four mild steels were installed in M-P-Z4 specimen, while O-P-Z4 specimen had six mild steels. Detailed information of specimens can be obtained from the reference (Cheok et al. 1993). Figures 11 and 12 present the moment—rotation curves of the tested hybrid joints

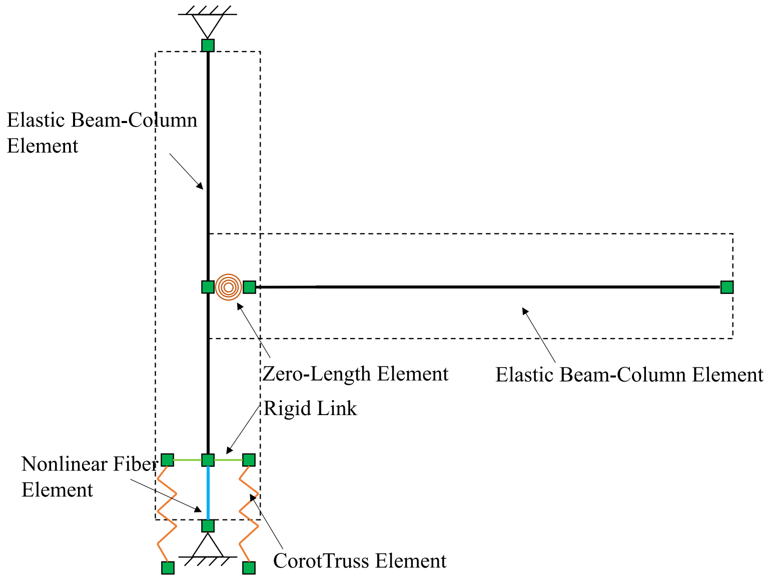

Fig. 10 Numerical model for hybrid joints in *OpenSees*

Table 15 Modal period of structures

Design example	T (s)	1st	2nd	3rd
Five-story SCCF	EBSD	1.13	0.64	0.48
	DDBD	1.12	0.62	0.48
Eight-story SCCF	EBSD	2.01	0.74	0.34
	DDBD	2.03	0.78	0.35

from the experimental data and numerical results. It shows that the strength, stiffness and the flag-shaped hysteretic behavior of hybrid joints with different mild steels under cyclic loads can be modeled well using the proposed numerical model.

4.2 Ground motions

Table 16 shows the summary of the 22 set far-field ground motions adopted in this study (FEMA 2009). Each set has 2 ground motion records in different directions. Thus, a total of 44 ground motion records were used in analyses.

4.3 Structural performance

To compare structural responses DI, θ_c, and θ_m with the design targets, nonlinear dynamic analyses are conducted on both the EBSD designed structures with 44 ground motions. According to the Chinese building code (2016), ground motions are scaled as $PGA = 220$ gal for the five-story SCCF and 400 gal for the eight-story SCCF, respectively. The results of DI, θ_c, and θ_m of all hybrid joints are listed in Table 17.

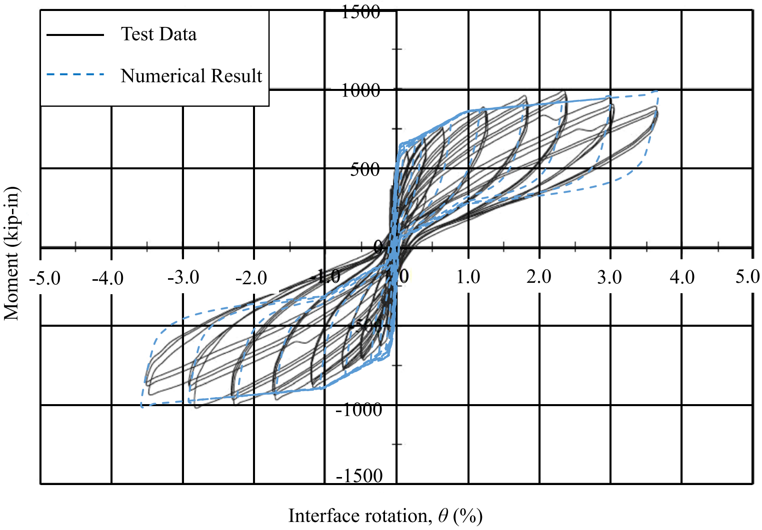

Fig. 11 Comparison of the numerical result with the test data of M-P-Z4

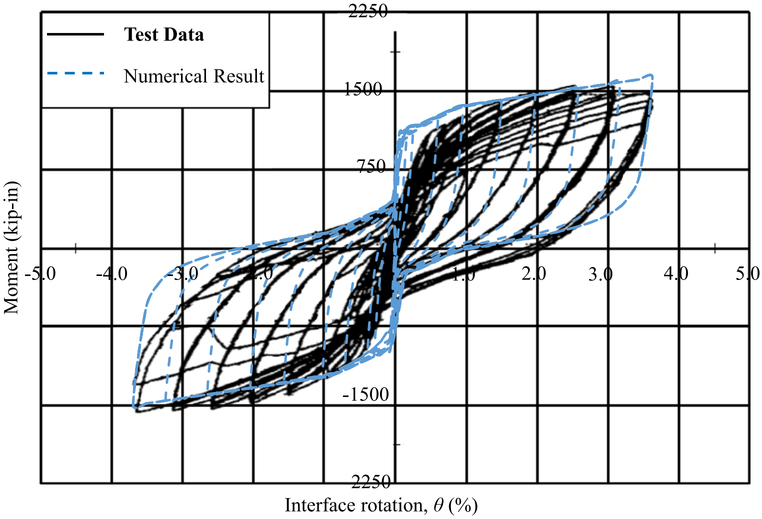

Fig. 12 Comparison of the numerical result with the test data of O-P-Z4

In the design procedure, DI = 0.5 was selected to limit the damage development for the repairable requirement after seismic actions. For the five-story SCCF, DI from all seismic actions is less than 0.5 except for three specific ground motion records, which satisfies with the repairable limit defined in Table 3. Meanwhile, damages developed in the eight-story SCCF surpass the repairable limit under only four ground motions. The mean values of DI under 44 seismic actions are 0.306 and 0.415, respectively. They are both smaller than the design target. Since the maximum of $E_{\mathrm{Hi,\ joint}}/E_{\mathrm{H,\ joint}}$ was adopted

Table 16 Detailed information of selected ground motions

No	Earthquake	Year	Station	Mw	Epicentral (km)	PGA (g)
1	Northridge	1994	Beverly Hills-Mulhol	6.7	13.3	0.52
2	Northridge	1994	Canyon Country-WLC	6.7	26.5	0.48
3	Duzce, Turkey	1999	Bolu	7.1	41.3	0.82
4	Hector Mine	1999	Hector	7.1	26.5	0.34
5	Imperial Valley	1979	Delta	6.5	33.7	0.35
6	Imperial Valley	1979	El Centro Array #11	6.5	29.4	0.38
7	Kobe, Japan	1995	Nishi-Akashi	6.9	8.7	0.51
8	Kobe, Japan	1995	Shin-Osaka	6.9	46	0.24
9	Kocaeli, Turkey	1999	Duzce	7.5	98.2	0.36
10	Kocaeli, Turkey	1999	Arcelik	7.5	53.7	0.22
11	Landers	1992	Yermo Fire Station	7.3	86	0.24
12	Landers	1992	Coolwater	7.3	82.1	0.42
13	Loma Prieta	1989	Capitola	6.9	9.8	0.53
14	Loma Prieta	1989	Gilroy Array #3	6.9	31.4	0.56
15	Manjil, Iran	1990	Abbar	7.4	40.4	0.51
16	Superstition Hills	1987	El Centro Imp. Co	6.5	35.8	0.36
17	Superstition Hills	1987	Poe Road (temp)	6.5	11.2	0.45
18	Cape Mendocino	1992	Rio Dell Overpass	7	22.7	0.55
19	Chi-Chi, Taiwan	1999	CHY101	7.6	32	0.44
20	Chi-Chi, Taiwan	1999	TCU045	7.6	77.5	0.51
21	San Fernando	1971	LA-Hollywood Stor	6.6	39.5	0.21
22	Friuli, Italy	1976	Tolmezzo	6.5	20.2	0.35

Table 17 Analytical results

	Five-story SCCF			Eight-story SCCF		
	DI	θ_c	θ_m	DI	θ_c	θ_m
Target	0.500	0.004	0.012	0.500	0.004	0.012
Minimum	0.067	0.001	0.009	0.104	0.001	0.008
Maximum	0.743	0.011	0.016	0.698	0.012	0.019
Mean	0.306	0.003	0.012	0.415	0.005	0.013
STD	0.129	0.002	0.002	0.115	0.002	0.003
Mean ± STD	0.435(0.177)	0.005(0.001)	0.014(0.010)	0.530(0.300)	0.007(0.003)	0.016(0.010)

in this paper to conservatively design the structure, the actual energy demand of each floor is less than the design value. As shown in Eq. (8), DI decreases with smaller $\int dE$, which leads to the numerical results less than design expectation. Nevertheless, according to Table 3, DI = 0.306 and 0.415 represent the moderate damage state, implying good agreement with the desired damage development. Meanwhile, θ_c and θ_m well match the target objectives determined during the EBSD design process. According to the standard deviations listed in Table 17, the discrepancy of quantified damages in hybrid joints is relatively bigger than that of deformation indexes. It indicates that damages developed in structures not only relate to structural features, but also ground motion characteristics. Damages formed in structures might vary greatly under different seismic actions.

Figure 13 presents statistical results of $E_{Hi,\ joint}/E_{H,\ joint}$ under 44 scaled ground motions for the EBSD designed five-story and eight-story SCCFs. It can be seen that the mean values of $E_{Hi,\ joint}$ / $E_{H,\ joint}$ are in good agreement with the predicted energy distribution listed in Tables 10 and 11. It indicates that the proposed method can reasonably quantify the distribution of energy demand in self-centering frame structures. On the other hand, great discrepancy in the energy distribution under different seismic actions can be observed according to statistical results (STD, MEAN + STD and MEAN–STD). It implies that the energy factor depends on both the structure features and earthquake characteristics.

Seismic fragility analyses are conducted on both examples designed using the EBSD and DDBD procedures. Figure 14 shows fragility curves of two designed structures corresponding to three limit states, including Immediate Occupancy (IO), Life Safety (LS) and Collapse Prevention (CP). These limit states are defined with the maximum deformation in accordance with minor earthquakes, DBE and MCE given in Table 4. It can be seen that for the same $S_a(T_1, 5\%)$, DDBD has higher probability of exceedance than EBSD on all three states considered in both design examples. This means that DDBD designed structures are likely to have more damages than the EBSD designed structures. Similarly, the differences of 50% exceedance probability between EBSD and DDBD designed five-story structure for IO, LS and CP are 0.12 g, 0.13 g, and 0.14 g, respectively for the five-story SCCF, while that of the eight-story structure are 0.9 g, 0.11 g and 0.14 g. This shows DDBD designed structures are more vulnerable. Since structural damages gradually develop and accumulate with bigger earthquakes, cumulative damages will have more significant effects on structural performance. Therefore, the EBSD designed structures exhibit better aseismic capacity, which results from the hysteretic energy considered in EBSD.

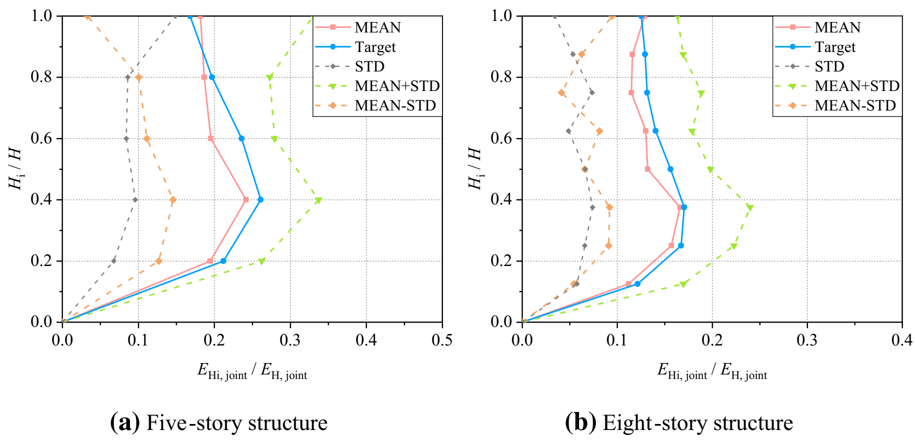

Fig. 13 Comparison of energy dissipation

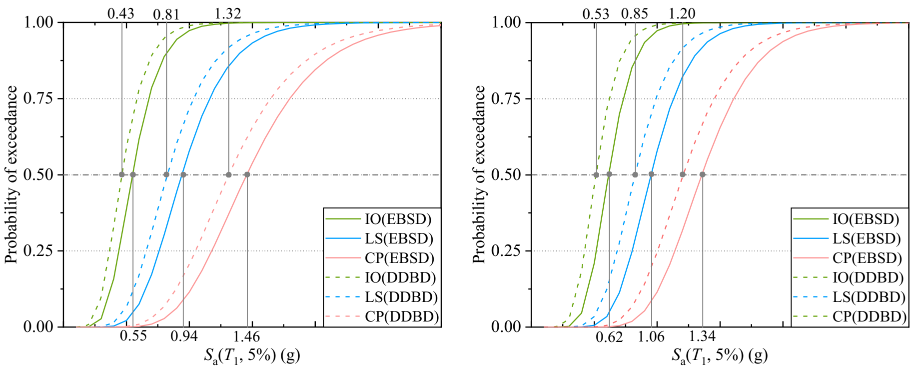

(a) Five-story structure

(b) Eight-story structure

Fig. 14 Comparison of fragility curves

5 Conclusions

To improve structural performance and optimize post-earthquake repairable capacity, self-centering frame structures have been developed. These systems exhibit excellent aseismic performance and resilient capacities, whereas existing design procedures cannot consider the effects of cumulative damages. This paper presents an energy-based seismic design (EBSD) procedure for self-centering concrete frame structures. Based on a proposed damage model, hysteretic energy demand E_H is introduced as a key design parameter to consider the effects of cumulative damages on structures. In addition, the damage state and structural deformation under the target earthquake intensity can be assigned. EBSD allows designers to select performance objectives for different seismic intensities corresponding to different structural performance targets. The detailed derivation of EBSD is illustrated in the paper. To demonstrate the applicability of EBSD, two SCCFs with different heights and hazard levels are designed and analyzed by nonlinear dynamic analyses. The results show that the EBSD designed structures exhibit better performance and more controlled damage than the DDBD. Meanwhile, the damage state and deformation responses well match the objectives determined during the EBSD design process. The results show that the well-designed structures satisfy with the repairable performance objective, which indicates significant source savings and downtime reduction for the structure after earthquakes.

Acknowledgements The authors are grateful for the financial support received from the National Key Research and Development Program of China (Grant No. 2016YFC0701101), National Natural Science Foundation of China (Grant No. 52025083, Grant No. 51778486), Shanghai Committee of Science and Technology (Grant No. 19DZ1201200) and China Scholarship Council during a visiting study in University of British Columbia (No.201906260206).

References

ACI Innovation Task Group 1 (2003) Special hybrid moment frames composed of discretely jointed precast and post-tensioned concrete members: ACI T1.2–03. Farmington Hill: American Concrete Institute

Akbas B, Shen J, Hao H (2001) Energy approach in performance-based seismic design of steel moment resisting frames for basic safety objective. Struct Des Tall Spec Build 10(3):193–217

Akiyama H (1985) Earthquake resistant limit state design for building. University of Tokyo Press, Tokyo, p 1985

Barbagallo F, Bosco M, Floridia A, Marino EM, Rossi PP (2020) Design for seismic upgrading of existing RC frames by friction dampers. Ingegneria Sismica 37(1):5–18

Bojorquez E, Ruiz SE, Teran A (2008) Reliability-based evaluation of steel structures using energy concepts. Eng Struct 30(6):1745–1759

Cai X, Pan Z, Zhu Y, Gong N, Wang Y (2021) Experimental and numerical investigations of self-centering post-tensioned precast beam-to-column connections with steel top and seat angles. Eng Struct 226:111397

Cheok G, Stone W, Lew HS (1993) Performance of 1/3-scale model precast concrete beam–column connections subjected to cyclic inelastic loads—report no. 3. NISTIR 5246, National Institute of Standards and Technology, NIST, Gaithersburg

Cheok G, Stone W (1994) Performance of 1/3-scale model precast concrete beam–column connections subjected to cyclic inelastic loads—report no. 4. NISTIR 5436, National Institute of Standards and Technology, NIST, Gaithersburg

Chou CC, Uang CM (2000) Establishing absorbed energy spectra – an attenuation approach. Earthq Eng Struct Dyn 29(10):1441–1455

Chou CC, Uang CM (2003) A procedure for evaluating seismic energy demand of framed structures. Earthq Eng Struct Dyn 32(2):229–244

Code for Seismic Design of Buildings [GB 50011–2010 (2016 Edition)] (2016) Ministry of Housing and Urban-rural Construction of the People's Republic of China

Cruz MF, Lopez OA (2000) Plastic energy dissipated during an earthquake as a function of structural properties and ground motion characteristics. Eng Struct 22(7):784–792

Decanini LD, Mollaioli F (1998) Formulation of elastic earthquake input energy spectra. Earthq Eng Struct Dyn 27(12):1503–1522

Du B, He Z, Huang GH (2019) An estimate on distribution of hysteretic energy demand in seismic precast concrete frame structures. J Earthq Eng. https://doi.org/10.1080/13632469.2019.1605950

El-Sheikh M, Sause R, Pessiki S, Lu LW (1999) Seismic behavior and design of unbonded post-tensioned precast concrete frames. PCI J 44(3):54–71

El-Sheikh M, Pessiki S, Sause R, Lu LW (2000) Moment rotation behavior of unbonded post-tensioned precast concrete beam–column connections. ACI Struct J 1:122–132

Fajfar P, Gaspersic P (1996) The N2 method for the seismic damage analyses of RC buildings. Earthq Eng Struct Dyn 25(1):31–46

FEMA P695 (2009) Quantification of building seismic performance factors Federal Emergency Management Agency Washington, DC

Housner GW (1959) Limit design of structures to resist earthquakes. Proceedings of the first world conference on earthquake engineering

Korkmaz HH, Tankut T (2005) Performance of a precast concrete beam-to-beam connection subject to reversed cyclic loading. Eng Struct 27(9):1392–1407

Lopez-Barraza A, E. Ruiz S, Reyes-Salazar A, Bojorquez E, (2016) Demands and distribution of hysteretic energy in moment resistant self-centering steel frames. Steel Compos Struct 20(5):1155–1171

NZS3101: 2006 (2006) Concrete Structures Standard: Part I - The design of concrete structures. Standards New Zealand, Wellington

NZS3101: 2006 (2006) Appendix B: special provisions for the seismic design of ductile jointed precast concrete structural systems. Standards New Zealand, Wellington

Pampanin S, Marriott D, Palermo A (2010) PRESSS design handbook. New Zealand Concrete Society Industry, Auckland

Park YJ, Ang HS (1985) Mechanistic seismic damage model for reinforced concrete. J Struct Eng 111(4):722–739

PEER (2000) Open system of earthquake engineering simulation (OpenSees). University of California, Berkeley, CA, Pacific Earthquake Engineering Research Center

Priestley MJN, Tao J (1993) Seismic response of precast prestressed concrete frames with partially debonded tendons. PCI J 38(1):58–69

Priestley MJN, Sritharan S, Conley JR, Pampanin S (1999) Preliminary results and conclusions from the PRESSS five-story precast concrete test building. PCI J 44(6):42–67

Priestley MJN (2002) Direct displacement-based design of precast/prestressed concrete buildings. PCI J 47(6):66–78

Song G, Yang TY, Zhou Y (2021) Distribution of hysteretic energy demands in self-centering concrete frame structures. Soil Dynam Earthq Eng 148:106828

Xue D, Bi K, Dong H, Qin H, Han Q, Du X (2021) Development of a novel self-centering slip friction brace for enhancing the cyclic behaviors of RC double -column bridge bents. Eng Struct 232:111838

The building Center of Japan (2005) Technological standard for earthquake-resistant calculation method for buildings based on energy balance. (in Japanese)

Tu BB, Zhao D (2018) Distribution of accumulated irrecoverable hysteretic energy in MDOF structures. Multidiscip Model Mater Struct 14(2):202–215

Uang CM, Bertero VV (1990) Evaluation of seismic energy in structures. Earthq Eng Struct Dyn 19(2):77–90

Wang B, Zhu S, Chen K, Huang J (2020) Development of superelastic SMA angles as seismic-resistant self-centering devices. Eng Struct 218:110836

Wang B, Nishiyama M, Zhu S, Tani M, Jiang H (2021) Development of novel self-centering steel coupling beams without beam elongation for earthquake resilience. Eng Struct 232:111827

Wu H, Sui Y, Zhou T, Huang B, Li X (2021) A novel self-centering energy-dissipating wall panel with framed beams as boundaries. Eng Struct 232:111864

Yang TY, Tung D, Li YJ (2018) Equivalent energy-based design procedure for earthquake resilient fused structures. Earthq Spectra 34(2):1–21

Yang TY, Atkinson J, Tobber L, Tung DP, Neville B (2020) Seismic design of outrigger systems using equivalent energy design procedure. Struct Des Tall Spec Build 29(10):e1743

Zhou Y, Song G, Huang SM, Wu H (2019a) Input energy spectra for self-centering SDOF systems. Soil Dynam Earthq Eng 121:293–305

Zhou Y, Song G, Tan P (2019b) Hysteretic energy demand for self-centering SDOF systems. Soil Dynam Earthq Eng 125: 105703

Zhou Y, Song G, Huang W (2020a) Performance-based damage evaluation of hybrid joints. B Earthq Eng 18:3781–3816

Zhou Y, Song G (2020b) Design energy spectra for self-centering SDOF systems. Earthq Eng Eng Dynam 40(2):1–12 (**(in Chinese**))